CFD-Guided Restoration of Occluded Schlieren Images for Supersonic Turbine Cascade Flow Diagnostics

Shihe Qu[1], Yizhou Duan[1], Zeyu Zheng[1], Xiubin Li[1], Yiwen Chen[2], Xiaomo Jiang[1], Xiaofang Wang[1], Yeming Lu[1,*]

[1]*Laboratory of Ocean Energy Utilization of Ministry of Education,School of Energy and Power Engineering, Dalian University of Technology, Dalian 116000, China*

[2]*State Key Laboratory of Clean and Efficient Turbomachinery Power Equipment, Deyang 618000, China*

Abstract: The operating environment of large-scale steam turbines is complex, and the flow characteristics around the long blades of the final stage are critical to both plant efficiency and safety. However, the fixed structure of ultra-thin blades causes occlusions in shadowgraph images, severely limiting precise analysis of flow characteristics. To this end, this paper proposes a physics-informed restoration framework specifically designed to overcome large-scale physical occlusions in ultra-thin blade cascade experiments. Distinct from general inpainting, our method achieves strict spatial coordinate synchronization between experimental and numerical domains via affine mapping, ensuring the reconstructed flow features are anchored to a consistent physical coordinate system. Combined with edge detection and feature recognition, occluded regions are localised, and numerical Schlieren information is utilised to reconstruct and repair these areas. Research findings demonstrate that this method effectively restores obscured regions, significantly improves the quality of the Schlieren image and provides reliable data support for in-depth analysis of flow characteristics of the final long blade cascade of steam turbines.

Keywords: Schlieren imaging; Supersonic cascade flow; CFD-assisted image restoration; Affine transformation; Edge detection.

1. INTRODUCTION

With the continuous demand for higher power output and efficiency in power generation systems, the aspect ratio of the final-stage blades in steam turbines has increased significantly. These blades, often exceeding one meter in length, operate in a complex environment that directly impacts the overall cycle efficiency and safety of the unit [1]. During operation, the final stage frequently encounters transonic and supersonic flow conditions characterized by high aerodynamic loading. Under these conditions, particularly at high angles of attack, the flow field within the cascade passage becomes extraordinarily intricate. Adverse aerodynamic phenomena, such as flow separation, shock-boundary layer interaction (SBLI), and shock wave oscillations, are prevalent [2, 3]. These complex flow nonlinearities not only challenge the structural integrity of the blades via aeroelastic instability but also impose strict requirements on the design and optimization of the turbomachinery [4].

To better understand these flow mechanisms and optimize blade design, flow visualization techniques are essential. Schlieren photography, a classic non-contact optical diagnostic method, is widely used to visualize density gradients in compressible flows based on the Gladstone-Dale relationship [5]. It effectively converts variations in fluid density into visible light intensity patterns, making it ideal for capturing shock waves and expansion fans. Numerous studies have employed Schlieren techniques to investigate cascade aerodynamics. For instance, recent experiments have combined high-speed Schlieren imaging with surface measurements to reveal the unsteady dynamics of shock oscillations in transonic turbine cascades [6] [7]. Others have utilized advanced setups, such as focusing Schlieren or Background Oriented Schlieren (BOS), to resolve three-dimensional flow features and verify the consistency between Computational Fluid Dynamics (CFD) predictions and experimental observations [8] [9].

Despite its extensive application, Schlieren visualization in high-load cascade experiments faces significant practical challenges. A primary issue is optical occlusion caused by the experimental apparatus itself. Due to the millimeter-level thickness and low stiffness of these blades, robust fixation structures are indispensable to prevent excessive deformation and aeroelastic instability [10]. However, these structural components, such as blade fixtures and latches, often obstruct the optical path, blocking critical regions of the

*Address correspondence to this author at Laboratory of Ocean Energy Utilization of Ministry of Education,School of Energy and Power Engineering, Dalian University of Technology, Dalian 116000, China;
E-mail: luyeming@dlut.edu.cn

Received on 19-01-2026 Accepted on 27-02-2026 Published on 4-03-2026

E-ISSN: 3110-9780/26

flow field [5]. This occlusion results in the loss of local flow information and introduces shadow distortions, which severely hampers the quantitative analysis of shock structures and flow separation.

Existing methods to address these image defects typically fall into two categories: hardware improvements and algorithmic restoration. Hardware approaches, such as optimizing light source placement or using calibration targets, can minimize artifacts but often lack flexibility and may introduce new interference [11]. Algorithmic approaches have evolved significantly. Recently, data-driven methods based on deep learning, such as Convolutional Neural Networks (CNN) and Physics-Informed Neural Networks (PINN), have shown promise in super-resolution reconstruction of turbulent flows [12] [13]. Some studies have even applied these techniques specifically to supersonic cascade flow fields. However, these learning-based methods typically require massive amounts of high-quality training data, which is often unavailable in scarce engineering experiments. Conventional image inpainting techniques often struggle to compensate for missing signal data [14]. However, conventional image inpainting techniques often struggle with the sharp gradients characteristic of shock waves, leading to blurring or artifacts in the reconstructed regions. Furthermore, most existing fusion techniques fail to fully exploit the physical consistency between experimental data and numerical simulations.

To address the limitations of existing methods, this paper proposes a novel Schlieren image restoration framework. While existing CFD-guided methods often rely on simple image blending or require massive training datasets , our approach utilizes CFD results as a physical skeleton through a rigid affine transformation. This establishes a direct mapping between the experimental optical path and the numerical flow domain, ensuring that the restoration of occluded shock waves is governed by aerodynamic consistency rather than mere visual continuity. This zero-shot approach is particularly advantageous for engineering experiments where high-quality training data is scarce. Subsequently, an edge-preserving diffusion algorithm is applied to reconstruct the occluded regions. This method effectively restores the continuity of shock waves and flow features without requiring complex hardware modifications, providing reliable data support for the aerodynamic analysis of ultra-long steam turbine final-stage blades.

2. IMAGE RECONSTRUCTION AND RESTORATION METHOD BASED ON FEATURE SPACE MAPPING AND NUMERICAL SCHLIEREN BENCHMARK

In repairing the Schlieren image of the final long blade of a transonic steam turbine, this method enhances image quality through key preprocessing steps, providing a foundation for analysing flow characteristics around the blade cascade. The experimental data were acquired from a 100 mm wide supersonic cascade test section containing 8 blades that form 7 flow passages. A standard transmission-type schlieren system was utilized, featuring a 300 mm diameter collimated beam produced by dual concave mirrors and a slit-type light source. A horizontal knife-edge was positioned at the focal point of the refocusing mirror to capture vertical density gradients. High-resolution images with a resolution of 2969 × 1980 pixels were recorded during the steady-state phase of the flow using a high-speed acquisition system.

2.1. Numerical Methodology

The numerical Schlieren benchmark, serving as the physical skeleton for the restoration framework, was obtained via a density-based RANS solver using the Transition SST turbulence model. The computational domain was discretized with a high-resolution structured mesh containing 5,961,200 elements. For the *Ma*=1.4 case, the boundary conditions were strictly matched with the experimental environment: a pressure inlet was applied with a total pressure of 222,637.8 Pa and a turbulence intensity of 5%, while the pressure outlet was set to a static gauge pressure of -509.5 Pa. All blade surfaces were modeled as stationary, no-slip, and adiabatic smooth walls with zero roughness height. These rigorous settings ensure that the numerical flow structures provide an aerodynamically consistent reference for image restoration.

To ensure the reliability of the CFD benchmark, a grid independence study was conducted across five mesh levels (2.18M to 10.22M elements). The mass-averaged exit Mach number was monitored as the convergence metric. As illustrated in Fig. **1**, the results stabilize significantly beyond 5.96 million elements, with a relative error of only 0.043% between the 5.96M and 10.22M cases. Consequently, the mesh with 5,961,200 elements was selected to balance computational efficiency and capture fidelity.

Grayscale conversion simplifies data while preserving critical features; Gaussian filtering reduces

noise and enhances image contrast; gradient enhancement accentuates edge details. These optimisations improve image quality and provide precise data for subsequent feature extraction, alignment, and restoration, ensuring process efficiency and reliability for accurate assessment of flow characteristics in final-stage long blades.

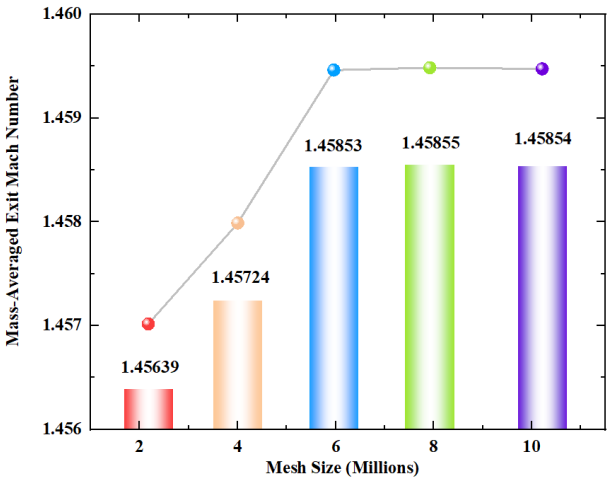

Figure 1: Grid independence study: mass-averaged exit Mach number across five mesh resolutions.

The specific implementation details of the proposed zero-shot cascade schlieren restoration framework are summarized in the pseudocode shown in Table **1**. The pseudocode emphasizes the iterative nature of the restoration, where the CFD-guided physical skeleton acts as a strict boundary constraint for the anisotropic diffusion process. This ensures that even with large-scale occlusions, the structural continuity of the shock waves is maintained while preventing unwanted artifacts during the texture propagation phase.

2.2. Image Preprocessing Workflow

As the primary stage in the image restoration workflow, image preprocessing plays a crucial role in determining the overall restoration outcome. Its core objective lies in optimising image quality, thereby establishing a foundation for subsequent complex feature extraction, precise image alignment, and meticulous restoration operations. Through greyscaling, specific weighted averaging algorithms map RGB colour image information into the greyscale domain, thereby achieving effective simplification of data dimensions. The mathematical expression for this process is shown in (1). This procedure not only substantially reduces computational complexity but also preserves core image features, facilitating efficient execution of subsequent processing steps.

Table 1: Pseudocode of the CFD-guided anisotropic diffusion restoration algorithm for enhancing Schlieren flow-field images.

Algorithm 1: CFD-Guided Anisotropic Diffusion Restoration

Input: Original experimental Schlieren image I_{exp}, numerical Schlieren benchmark I_{num} , and feature control point set P.

Output: Restored high-quality flow field image $I_{restored}$.

// **Stage 1**: Multi-scale Image Preprocessing
$I_{gray} \leftarrow$ Convert I_{exp} to grayscale using weighted averaging
$I_{smooth} \leftarrow$ Apply Gaussian filtering for noise suppression (σ = 1.0)
$I_{grad} \leftarrow$ Enhance edge details using the Sobel operator with scaling factor 1.5
// **Stage 2:** Feature-Space Affine Alignment
$\{A, t\} \leftarrow$ Compute optimal transformation matrix via Least Squares .
Ialign $\leftarrow$ Map experimental texture to numerical domain via affine transformation.
// **Stage 3**: Boundary Extraction and Blur Recognition.
Bnum $\leftarrow$ Extract numerical boundaries via multi-scale gradient analysis.
Sboundary $\leftarrow$ Apply directional scanning for coherent geometric topology.
$D(x, y) \leftarrow$ Generate distance transform from nearest boundary points.
$F(x, y) \leftarrow$ Calculate blur feature function $F = \alpha (1 - G) + \beta D$.
Rblur $\leftarrow$ Identify occluded regions where $F(x, y) \geq T_f$.
// **Stage 4**: Physical-Skeleton Guided Diffusion Restoration
$I^{(0)} \leftarrow$ Ialign; set time step Δt = 0.2 and iterations n_{max} = 100.
for n = 0 to n_{max} - 1 do.
$\nabla I^{(n)} \leftarrow$ Compute discrete gradients in x and y directions.
$c \leftarrow$ Calculate anisotropic diffusion coefficient $g(|\nabla I|)$.
foreach pixel $(x, y) \in I$ do
if $(x, y) \in$ Rblur then // Restore occluded region via CFD guidance
$I^{(n+1)} \leftarrow I^{(n)} + \Delta t \cdot \mathrm{div}(c \cdot \nabla I^{(n)})$
else // Preserve original experimental texture
$I^{(n+1)} \leftarrow I^{(n)}$
end if
end for
end for
return $I_{restored} \leftarrow I^{(nmax)}$.

$$I_{gray} = 0.299 \times I_{red} + 0.587 I_{green} + 0.114 I_{gray} \quad (1)$$

In the formula, I is used to denote the intensity value or brightness value of a particular pixel in an image.

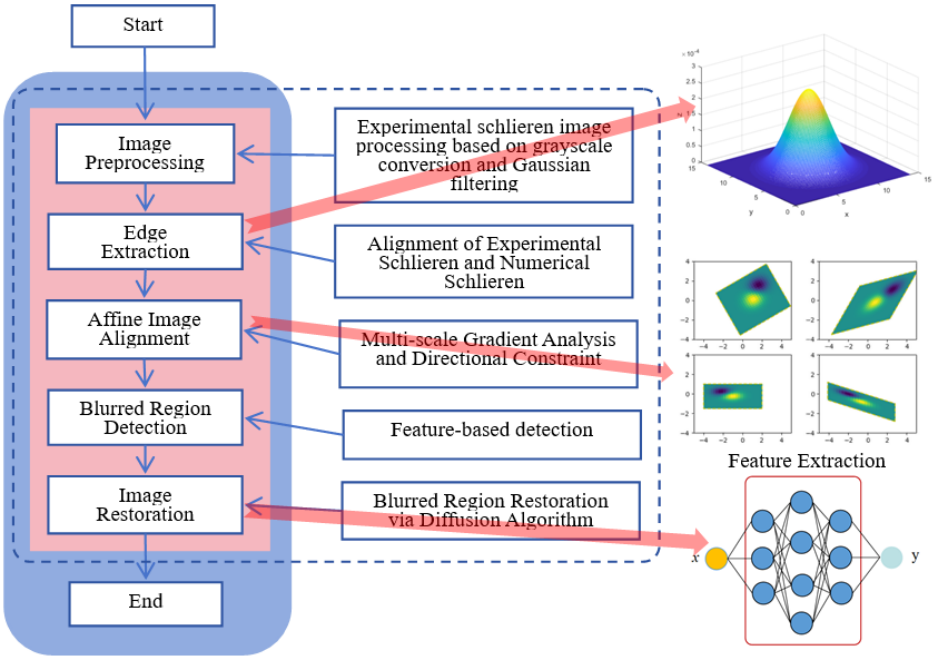

Figure 2: Flowchart of the proposed Schlieren image restoration framework.

Building upon this foundation, further noise filtering processing is undertaken to eliminate random noise interference within the images. This study employs a Gaussian filter, whose mathematical expression is shown in (2) below. By applying a convolution operation to the images, and leveraging the smoothing properties of the Gaussian function, the noise components are effectively suppressed while maximally preserving critical image details and features.

$$I_{filtered}(x,y) = \frac{1}{2\pi\sigma^2}\int_{-\infty}^{\infty}\int_{-\infty}^{\infty} I(x',y')\, e^{-\frac{(x-x')^2+(y-y')^2}{2\sigma^2}} dx'dy' \tag{2}$$

Herein,$I_{filtered}(x,y)$ denotes the pixel value of the filtered image at position (x, y) ,and $I(x^{'},y^{'})$ represents the pixel value of the original image at position (x', y') ,and σ denotes the standard deviation of the Gaussian function, which determines the smoothing effect of the filter.

In this study, a 5×5 Gaussian kernel with a standard deviation of σ = 1.0 is employed for noise suppression. These parameters are chosen to strike an optimal balance between filtering high-frequency random noise from the high-speed camera and preserving the sharp density gradients of the shock waves. Following the filtering, a Sobel operator is applied for gradient enhancement with a scaling factor of 1.5. This setting is justified as it accentuates subtle flow structures in the expansion regions without introducing excessive artifacts that could interfere with subsequent feature recognition.

2.3. Principles of Affine Transformation Methods

The affine transformation is utilized here as a rigorous coordinate-level synchronization tool rather than a simple image registration technique. In ultra-thin blade tests, the necessary robust external supports create substantial occlusions. Our model corrects for perspective and installation offsets to transform the experimental texture into the exact numerical domain. This step is fundamental to our method's novelty, as it ensures that the subsequent anisotropic diffusion propagates flow information along the physically correct shock wave trajectories defined by the CFD benchmark. Affine transformation is a two-dimensional geometric transformation, expressed as Eq. (3):

$$\begin{bmatrix} x^{'} \\ y^{'} \end{bmatrix} = A\begin{bmatrix} x \\ y \end{bmatrix} + \begin{bmatrix} t_x \\ t_y \end{bmatrix} \tag{3}$$

Herein,(x,y) and$(x^{'},y^{'})$ denote the point coordinates before and after transformation respectively, A represents a 2x2 transformation matrix, and t is the translation vector.

In this study, the corresponding control points are manually selected based on stable geometric features and high-gradient flow structures. Specifically, 8 pairs of characteristic points are identified, including the

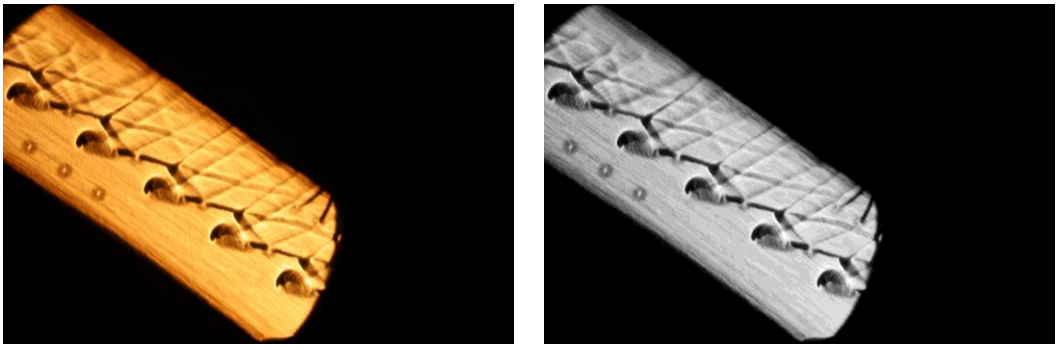

(a) Original experimental Schlieren map (b) Experimental Schlieren image after preprocessing

Figure 3: Comparison of image preprocessing results.

leading and trailing edge tips of the blades and specific coordinates on the cascade sidewall. Manual selection is preferred here over automatic matching (like SIFT or ORB) because the experimental Schlieren and numerical images exhibit significant differences in texture and noise levels, making automated feature descriptor matching less robust. The robustness of this alignment is ensured by using the least squares method to minimize the global residual error, ensuring that the local manual selection leads to a globally consistent coordinate mapping. The solution to affine transformations is typically achieved through the method of least squares, which minimises the error between corresponding points before and after the transformation. The objective of the least squares method is to find the optimal transformation matrix A and translation vector *t*, such that the error function is minimised:

$$E(A, t_x, t_y) = \sum_{i=1}^{n} \left((x_i' - (A \begin{bmatrix} x_i \\ y_i \end{bmatrix} + \begin{bmatrix} t_x \\ t_y \end{bmatrix}))^2 + (y_i' - (A \begin{bmatrix} x_i \\ y_i \end{bmatrix} + \begin{bmatrix} t_x \\ t_y \end{bmatrix}))^2 \right) \quad (4)$$

Herein,(x, y) and(x', y') denote corresponding points in the experimental Schlieren and numerical Schlieren respectively,n represents the number of points,the result of the affine transformation alignment is shown in Fig. **3**.

To quantitatively validate the alignment precision, eight physical landmarks were selected as control points, as illustrated in Fig. **4**. The Euclidean distances between the synchronized experimental and numerical coordinates were measured and are summarized in Table **2**. The Euclidean distances between the synchronized experimental and numerical coordinates were measured and are summarized in Table **2**. The results show that the Root Mean Square Error (RMSE) is 3.28 pixels. Considering the image width resolution of 2969 pixels, the relative spatial error is approximately 0.11%. This sub-pixel level alignment precision ensures that the restored geometry is anchored to a mathematically consistent physical coordinate system, providing a rigorous foundation for the restoration process.

2.4. Boundary Extraction from Numerical Schlieren Images Based on Gradient Information and Directional Constraints

In the process of image reconstruction and restoration, edge detection serves as a critical step for precisely locating occluded areas. This paper proposes an enhanced edge detection method, centred on employing multi-scale gradient analysis and adaptive threshold segmentation techniques to accurately capture boundary information within numerical

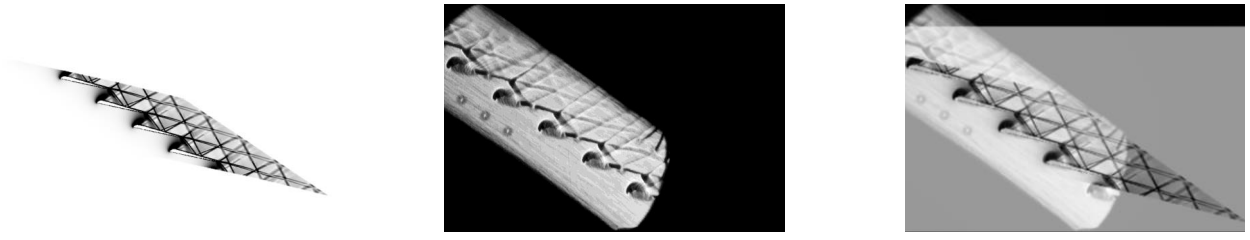

(a) Numerical Schlieren Plot (b) Experimental Schlieren pattern (c) Affine Image Alignment

Figure 4: Alignment results.

Table 2: Quantitative analysis of feature point residuals after affine transformation.

Feature Point ID	Landmark Location	Experimental Coord. (*x*, *y*)	Numerical Coord. (*x'*, *y'*)	Distance Error
1	Leading Edge of 1st Blade	(108, 522)	(108, 524.7)	2.70
2	Leading Edge of 2nd Blade	(510, 803)	(507, 799)	5.00
3	Leading Edge of 3rd Blade	(900.6, 1075.6)	(902, 1074)	2.13
4	Leading Edge of 4th Blade	(1287.4, 1345.8)	(1286.6, 1343.7)	2.25
5	Trailing Edge of 1st Blade	(674, 648)	(677, 648)	3.00
6	Trailing Edge of 2nd Blade	(1066, 925)	(1070, 928)	5.00
7	Trailing Edge of 3rd Blade	(1145.8, 1187.7)	(1145, 1187)	1.06
8	Trailing Edge of 4rd Blade	(1837, 1467.1)	(1839, 1469.3)	2.97

Schlieren images, providing a reliable foundation for subsequent restoration of occluded areas.

The core of this strategy lies in constructing a detection function capable of adaptively capturing pixel-level abrupt changes in grey-scale values. By integrating local gradient information, it achieves efficient identification and precise localisation of boundaries within numerical Schlieren images. Specifically, the numerical Schlieren image is first subjected to binarisation based on local gradient information, thereby establishing the following boundary feature extraction function:

$$S(x,y)=\begin{cases}1, \nabla I_{num}(x,y) \geq \tau \cdot max(\nabla I_{num}) \\ 0, \quad otherwise\end{cases} \tag{5}$$

Herein, $I_{num}(x,y)$ denotes the grey-value distribution matrix of the numerical Schlieren image, and ∇represents the gradient operator,which is used tocapture local rates of change in grey values within the image. In this study, the parameters are set as τ = 0.15 and θ= 0.2. These values are determined through a sensitivity analysis where τ was varied from 0.05 to 0.3. It was observed that the extracted boundary remains stable within τ∈[0.1, 0.2], with pixel-level deviations less than 1.5%, indicating low sensitivity to parameter fluctuations. For the directional constraint θ, a value of 0.2 effectively filters high-frequency numerical oscillations while preserving the coherent topology of the shock waves. Importantly, these parameters remain constant across both Ma = 1.4 and Ma = 1.5 cases, demonstrating the robust generalization of the boundary extraction method across different flow intensities.

Building upon this foundation, a directional scanning algorithm is introduced, which starts from the starting point on the left boundary of the image and performs pixel-by-pixel state transition detection along the predefined scanning path. When the pixel's state is detected to satisfy the following conditions, that pixel is determined to belong to the left boundary set. Its mathematical expression is shown in (6):

$$\Delta S(x,y)=S(x+1,y)-S(x,y)=1 \tag{6}$$

Herein,$\Delta S(x,y)$ represents the binary state transition between adjacent pixels,while $\partial S/\partial X$ further employs partial derivatives to constrain the directionality of boundary extraction, ensuring the extracted boundaries possess coherent geometric topology.The parameterθserves as a directional gradient threshold to suppress spurious feature points on non-boundaries. The boundary extraction results for the numerical shadow image are illustrated in Fig. **3**.

2.5. Blurred Region Recognition for Feature-Based Detection for Feature-Based Detection

Following the extraction of the left boundary from the numerical shadow image, we utilise these boundary features to guide the identification of blurred regions[15]. Boundary information not only provides clear region separation but also indicates potential blurred areas that may be affected by occlusion or deformation. First, we define a blurred feature function *F*(*x, y*) to measure the occlusion probability. The physical rationale for combining gradient magnitude and distance-to-boundary is that physical occlusions typically manifest as artificial smooth regions with low gradient intensity, specifically concentrated near the physical interfaces of the cascade. By incorporating the distance term *D*, the model effectively distinguishes these structural occlusions from the naturally smooth flow regions in the mainstream. Furthermore, the recognition threshold T_f is chosen adaptively based on the root-mean-square (RMS) of the gradient values within the unobstructed

numerical domain. This ensures the threshold remains robust across different flow conditions where the baseline gradient levels of the shock waves fluctuate. This function combines gradient information and boundary information, with its mathematical expression given by (7):

$$F(x,y) = \alpha \cdot (1 - G(x,y)) + \beta \cdot D(x,y) \quad (7)$$

Herein,$G(x,y)$ denotes the normalised gradient magnitude, reflecting the edge strength at that point in the image；$D(x,y)$ represents the distance from that point to the nearest boundary, obtained via a distance transformation；$\alpha$and $\beta$are weighting coefficients used to balance the influence of gradient and distance, satisfying α+β=1.

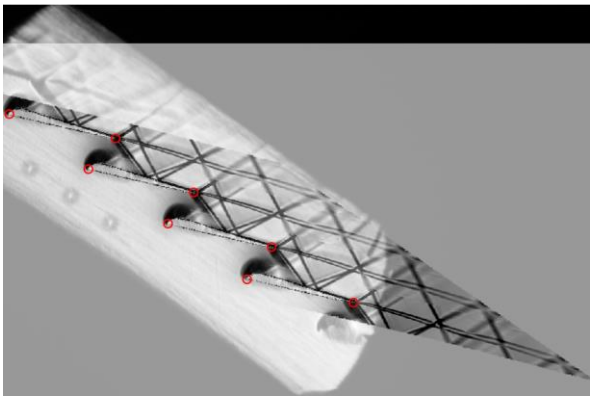

Figure 5: Distribution of feature points for quantitative alignment verification.

Through the blur feature function *F*(*x, y*),blurred regions within an image can be effectively identified. Areas exhibiting lower gradient magnitudes typically correspond to smooth regions or blurred boundaries in the image, Consequently, 1-*G*(*x*, *y*) is employed to highlight these potential blurred areas. The distance transform provides information on the distance from each pixel to the nearest boundary, aiding in the identification of gradient regions near boundaries—areas where blurring effects typically manifest most prominently. Based on this blur feature function, we can determine blurred regions by setting a threshold T_f:

$$R_{blue} = \{(x,y) | F(x,y) \geq T_f\} \quad (8)$$

Herein, R_{bule} denotes the set of identified fuzzy regions; T_f represents the fuzzy recognition threshold, whose value is determined based on the specific characteristics of the image and experimental requirements, the recognition results of the blur feature function *F*(*x, y*) are shown in Fig. **5**.

3. IMAGE RESTORATION AND COMPARISON OF RESULTS

3.1. Restoration of Fuzzy Regions Based on Diffusion Algorithms

Based on the blurred regions detected through the aforementioned features, image restoration is performed using a diffusion algorithm, with reference to surrounding area information[16]. Specifically, the restoration process first precisely locates the blurred regions requiring repair within the image based on the characteristics of the blur feature function *F*(*x, y*) .A restoration mask is then constructed with the boundaries of this region as its core. Within the restoration mask, the fusion of numerical and experimental information is achieved via topological guidance rather than direct pixel replacement. Specifically, the numerical Schlieren image serves as a gradient prior, defining the anisotropic diffusion coefficients and directions. This ensures that the healthy experimental texture from the periphery is propagated along the physically correct shock wave trajectories provided by the CFD benchmark. Consequently, the restored region is a weighted synthesis where the structural topology is governed by the CFD physics, while the fine-scale texture and noise characteristics are inherited from the surrounding experimental data. This enables the gradual restoration of details and structures consistent with the surrounding environment. The fundamental principle of the diffusion algorithm involves the diffusion of gradient information within the blurred region, following the

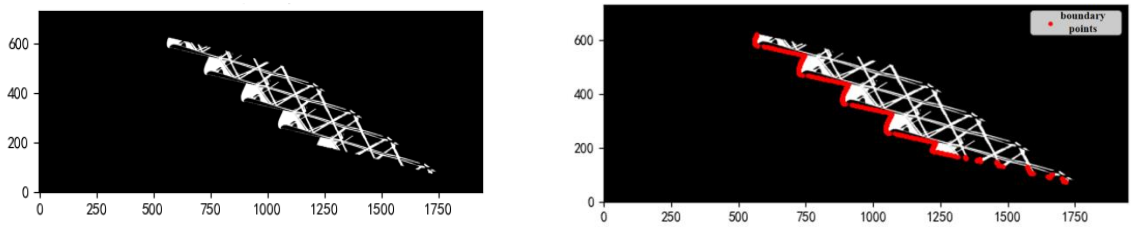

(a) Original numerical Schlieren binary image

(b) Boundary detection image

Figure 6: Numerical Schlieren Boundary Detection.

process outlined in Eq. (9). This formulation is derived from the foundational anisotropic diffusion model proposed by Perona and Malik[17], which effectively inhibits diffusion across edges to preserve structural details while smoothing homogeneous regions.

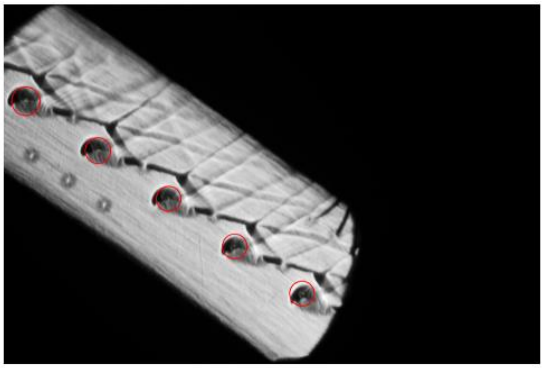

Figure 7: Fuzzy area recognition.

$$\frac{\partial I}{\partial t} = \nabla \cdot (c(|\nabla I|)\nabla I) \tag{9}$$

Herein, I denotes the grey-scale value of the image,t represents the diffusion time (number of iterations),$c(|\nabla I|)$ is the diffusion coefficient, determined by the magnitude of the image gradient.The value of the diffusion coefficient dictates the intensity and direction of diffusion. Typically, the diffusion coefficient is reduced in regions of high gradient (such as edges) to preserve edge information, while it is increased in regions of low gradient (such as smooth areas) to accelerate the repair process.

3.1.1. Gradient Computation

Gradient computation forms the foundation of diffusion algorithms, serving to determine the gradient information for each pixel in an image, encompassing both magnitude and direction. Gradient calculation can be achieved through the Sobel operator or other gradient operators. Gradient calculation can be achieved through various discrete differentiation operators. This paper employs the classic Sobel operator[18], which is robust in detecting edges in noisy environments. Its definition is shown in (10):

$$G_x = \begin{bmatrix} -1 & 0 & 1 \\ -2 & 0 & 2 \\ -1 & 0 & 1 \end{bmatrix}, G_y = \begin{bmatrix} -1 & -2 & -1 \\ 0 & 0 & 0 \\ 1 & 2 & 1 \end{bmatrix} \tag{10}$$

For each pixel point (x, y) in image I, its gradients in the x and y directions are shown in Eq. (11):

$$|\nabla I_x| = \sqrt{(\nabla I_x)^2 + (\nabla I_y)^2}, \theta = arctan(\frac{\nabla I_x}{\nabla I_y}), \tag{11}$$

3.1.2. Determination of Diffusion Direction

The direction of diffusion is determined based on gradient information, with priority given to diffusion along directions of smaller gradient to reduce damage to the edge. The diffusion coefficient $c(|\nabla I|)$ determines the intensity and direction of diffusion, defined as follows in (12):

$$c(|\nabla I|) = exp(-\frac{(|\nabla I|)^2}{2k^2}) \tag{12}$$

In this study, the gradient threshold *k* is set to 20, a value chosen based on the noise floor of the preprocessed experimental images to effectively distinguish flow gradients from background fluctuations. For the iterative updates, a total of *n* = 100 iterations are performed to ensure sufficient convergence of the gray-scale field within the occlusion mask. To maintain numerical stability during the explicit integration of the diffusion equation , the time step Δ*t* is strictly set to 0.2. This choice satisfies the Courant-Friedrichs-Lewy (CFL) stability condition for 2D anisotropic diffusion, which requires $\Delta t \leqq 0.25$ to prevent numerical oscillations and ensure the stability of the second-order spatial operator.

3.1.3. Information Transmission

Information transfer constitutes the core step of the diffusion algorithm, conveying texture and structural information from surrounding healthy regions to blurred areas via the diffusion equation. The diffusion equation is expressed as follows (13):

$$\frac{\partial I}{\partial t} = \nabla \cdot (c(|\nabla I|)\nabla I) \tag{13}$$

In discrete form, it can be expressed as (14):

$$I(x, y, t + \Delta t) = I(x, y, t) + [\nabla \cdot (c(|\nabla I|)\nabla I] \tag{14}$$

Herein, Δ*t* is the time step, typically set to a small value to ensure numerical stability.

3.1.4. Iterative Updates

Iterative updates involve repeating the aforementioned diffusion process until the fuzzy region is fully repaired or a predetermined number of iterations is reached. The formula for each iterative update is shown in (15):

$$I^{(n+1)}(x, y) = I(x, y, t) + \Delta t[\nabla \cdot (c(|\nabla I|)\nabla I] \tag{15}$$

Herein, I^n represents the image after the nth iteration, $I^{(n+1)}$ represents the image after the (*n+1*)th iteration.

3.2. Blurred Area Image Restoration

Based on image preprocessing, affine alignment, boundary extraction, and blurred region identification, the restoration performance under the baseline condition of *Ma* = 1.4 is illustrated in Fig. **6**. Following the restoration, the density gradient at the shock root seamlessly connects with the upstream distribution, while the shock's geometric features remain intact.

To further demonstrate the robustness of the proposed framework, an additional validation case was conducted at a higher Mach number of Ma = 1.5, as shown in Fig. **7**. Compared to the Ma = 1.4 case, the shock wave at Ma = 1.5 exhibits a larger inclination angle and higher density gradient intensity. Despite these topographical changes in the flow field, the affine transformation successfully maintained precise spatial alignment, and the anisotropic diffusion algorithm effectively reconstructed the occluded regions. These results confirm that the framework is robust and generalizable across different supersonic flow regimes.

3.3. Quantitative Evaluation of Boundary Gradient Continuity

To move beyond qualitative visual comparison, a quantitative analysis of gradient continuity was performed at the restoration interface. Figure **8**(**a**) illustrates the sampling path perpendicular to the restored blade edge. The resulting intensity distribution curve in Fig. **8**(**b**) exhibits a monotonic and smooth S-curve transition from the experimental gray-scale background to the numerical black blade body.

Quantitatively, this transition occurs over a span of approximately 8–10 pixels rather than a single-pixel step-change, which confirms that the anisotropic diffusion algorithm successfully integrated the numerical geometry while maintaining physical continuity. The absence of artificial intensity spikes or ringing artifacts at the boundary demonstrates that the restored geometric skeleton is seamlessly blended with the experimental texture at a sub-pixel level.

3.4. Discussion on CFD Dependency and Over-correction Risk

It is important to note that the proposed framework utilizes CFD results as a physical skeleton to guide the restoration. While this ensures aerodynamic consistency, it introduces a potential risk of over-correction or CFD-induced bias. If the numerical simulation fails to capture certain off-design flow features, the restored image may artificially mirror these omissions. To mitigate this, our method restricts the diffusion process strictly within the identified occlusion mask, preserving the original experimental texture in all unobstructed regions. Furthermore, the anisotropic diffusion algorithm is designed to propagate

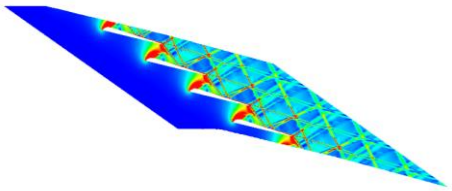

(a) Numerical Density Gradient

(b) Numerical Schlieren Plot

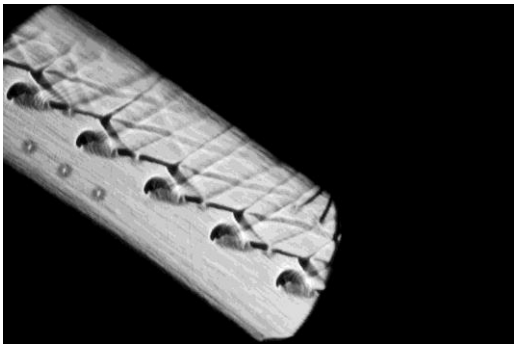

(c) Experimental Schlieren image before restoration

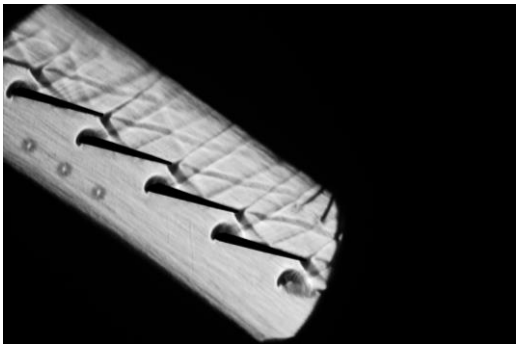

(d) Experimental Schlieren image after restoration

Figure 8: Comparison of experimental Schlieren images before and after restoration at *Ma* = 1.4.

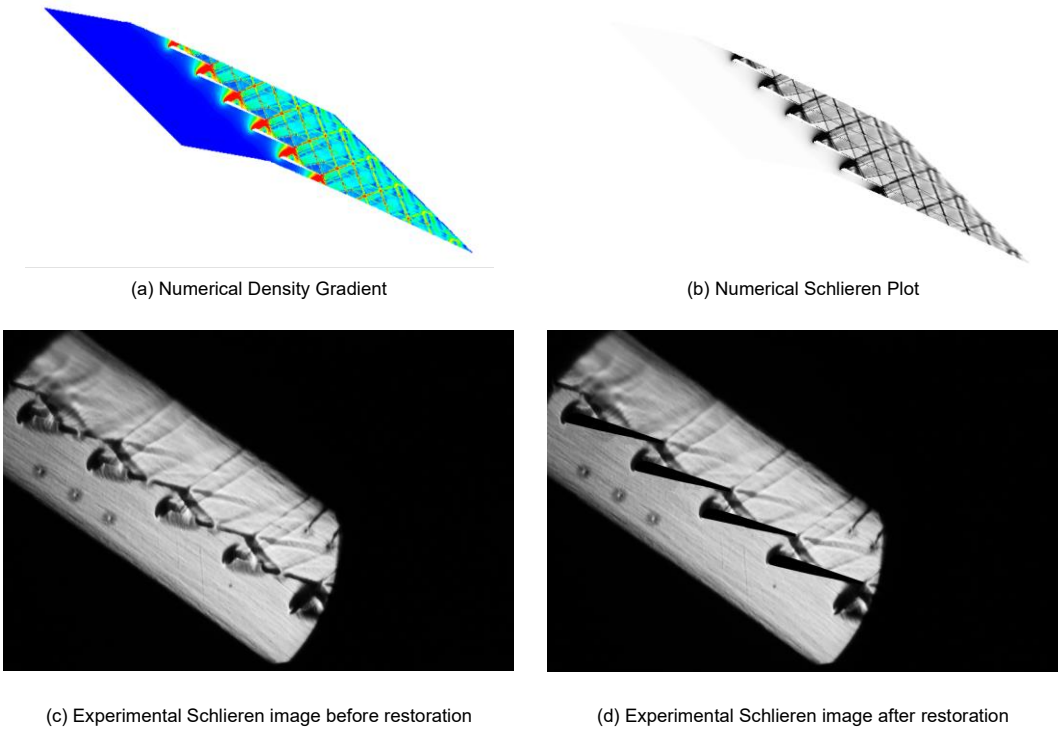

(a) Numerical Density Gradient (b) Numerical Schlieren Plot

(c) Experimental Schlieren image before restoration (d) Experimental Schlieren image after restoration

Figure 9: Comparison of experimental Schlieren images before and after restoration at *Ma* = 1.5.

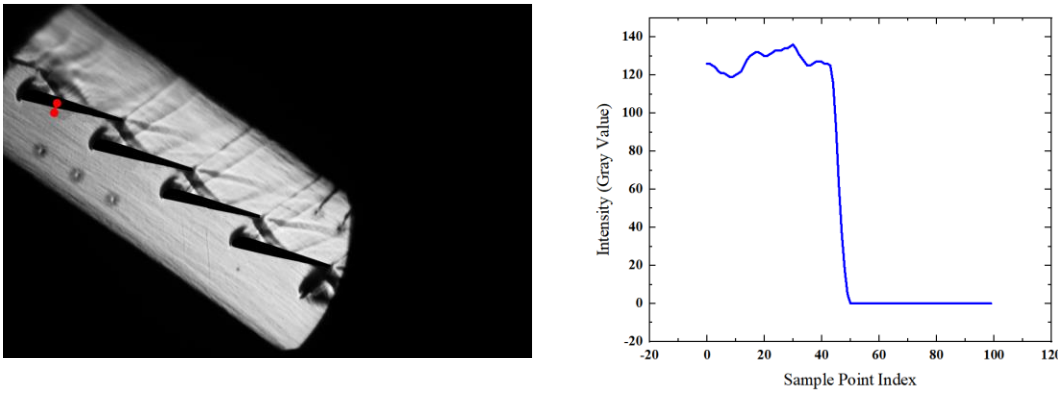

(a) Perpendicular sampling location across the blade edge (b) Intensity distribution curve

Figure 10: Quantitative evaluation of boundary gradient continuity.

information rather than perform direct pixel replacement, ensuring a smooth transition between the CFD-guided zones and the experiment-dominant zones.

3. CONCLUSION

This paper addresses the critical issues of grey-scale information loss and density gradient distortion. These defects are caused by occlusion in supersonic cascade Schlieren images, particularly regarding the final-stage long blades of large-capacity steam turbines. To resolve this, a comprehensive restoration framework was proposed and fully implemented. This framework integrates Feature Affine Transformation, Numerical Schlieren Reference, and Anisotropic Diffusion.

(1) A comprehensive processing pipeline was established, integrating greyscaling, Gaussian filtering, and Sobel gradient enhancement. This approach effectively suppresses random noise while significantly enhancing critical edge and structural information. Subsequently, an affine transformation model based on the least squares method was applied to align experimental flow field images with CFD numerical Schlieren benchmarks. This alignment ensures strict

spatial correspondence between occluded regions and unobstructed reference areas. Ultimately, this lays a robust foundation for subsequent image restoration.

(2) Multi-scale gradient analysis was employed in conjunction with directionally constrained boundary extraction. This combination allows for the adaptive capture of boundary information, thereby precisely delineating the extent of occlusion within Schlieren images. This process provides accurate regional demarcation for subsequent restoration. It ensures that restoration efforts are confined solely to the areas requiring intervention. As a result, both the targeting and efficiency of the restoration process are significantly enhanced.

(3) An anisotropic diffusion algorithm was employed to restore the identified occluded regions. During this process, the algorithm intelligently adjusts diffusion direction and intensity based on image gradient information. This mechanism ensures that critical details are effectively preserved. The restored image exhibits a continuous density gradient. Moreover, its streamline topology remains highly consistent with numerical simulation results, meeting the accuracy requirements for supersonic cascade flow diagnosis. Notably, this method requires no additional hardware, relying solely on image processing software and CFD data. Consequently, it offers significant economic and reliability advantages, making it readily applicable for engineering practice.

ACKNOWLEDGMENTS

This work is supported by the National Natural Science Foundation of China (No.U2541267), the Fundamental Research Funds for the Central Universities (No.DUT25LAB110), the State Key Laboratory of Clean and Effcient Turbomachinery Power Equipment (No.DEC8300CG202511985A1228194).

REFERENCES

[1] Hoznedl M, Sedlák K. Experimental And Numerical Research on Flow in the Last Stage of 1090mw Steam Turbine[J]. 2018.

[2] Papagiannis I, Raheem A, Basol A, *et al*. Unsteady flow mechanisms in the last stage of a transonic low pressure steam turbine—multistage effects and tip leakage flows[J]. Journal of the Global Power and Propulsion Society, 2017, 1: 95-112.

[3] Börner M, Niehuis R. Dynamics of shock waves interacting with laminar separated transonic turbine flow investigated by high-speed Schlieren and surface hot-film sensors[J]. Journal of Turbomachinery, 2021, 143(5): 051010.

[4] He L. Fourier methods for turbomachinery applications[J]. Progress in Aerospace Sciences, 2010, 46(8): 329-341.

[5] Settles G S. Schlieren and shadowgraph techniques: visualizing phenomena in transparent media[M]. Springer Science & Business Media, 2001.

[6] Halby A, Cakir B O, Da Valle L, *et al*. On the Application of Background Oriented Schlieren to a Transonic Low-Reynolds Turbine Cascade[J]. Journal of Turbomachinery, 2025, 147(5): 051016.

[7] Passmann M, aus der Wiesche S, Joos F. Focusing Schlieren visualization of transonic turbine tip-leakage flows[J]. International Journal of Turbomachinery, Propulsion and Power, 2020, 5(1): 1.

[8] Hargather M J, Settles G S. A comparison of three quantitative Schlieren techniques[J]. Optics and Lasers in Engineering, 2012, 50(1): 8-17.

[9] Chen L, Zhang Y, Xue H, *et al*. Experimental and numerical investigation of shock wave/boundary layer interactions induced by curved back-swept compression ramp[J]. Aerospace Science and Technology, 2023, 142: 108639.

[10] Zheng Z, Lu Y, Qu S, *et al*. A study of the correlation between FSI flow behaviors and losses for the supersonic turbine cascade with millimeter-level ultra-thin blades and a high inlet flow angle[J]. Aerospace Science and Technology, 2026: 111700.

[11] Raffel M. Background-oriented Schlieren (BOS) techniques[J]. Experiments in Fluids, 2015, 56(3): 60.

[12] Fukami K, Fukagata K, Taira K. Super-resolution reconstruction of turbulent flows with machine learning[J]. Journal of Fluid Mechanics, 2019, 870: 106-120.

[13] Ekwonu M C, Zhang S, Chen B, *et al*. Super-resolution reconstruction of schlieren images of supersonic free jets based on machine learning with bubble shadowgraphy data[J]. Journal of Visualization, 2023, 26(5): 1085-1099.

[14] Ram V S, de Rubeis T, Ambrosini D, *et al*. Deep learning approach for flow visualization in background-oriented Schlieren[J]. Applied Optics, 2025, 64(27): 7938-7947.

[15] Tang C, Zhu X, Liu X, *et al*. Defusionnet: Defocus blur detection via recurrently fusing and refining multi-scale deep features[C]//Proceedings of the IEEE/CVF conference on computer vision and pattern recognition. 2019: 2700-2709.

[16] Barbu T. Nonlinear diffusion-based image restoration models[M]//Novel diffusion-based models for image restoration and interpolation. Cham: Springer International Publishing, 2018: 25-82.

[17] Perona P, Malik J. Scale-space and edge detection using anisotropic diffusion[J]. IEEE Transactions on pattern analysis and machine intelligence, 2002, 12(7): 629-639.

[18] Kanopoulos N, Vasanthavada N, Baker R L. Design of an image edge detection filter using the Sobel operator[J]. IEEE Journal of solid-state circuits, 1988, 23(2): 358-367.

https://doi.org/10.66000/3110-9780.2026.02.02